










Velocity-space Signatures of Resonant Energy Transfer between Whistler Waves and Electrons in the Earth's Magnetosheath

Wence Jiang^{1,2,3} , Daniel Verscharen² , Seong-Yeop Jeong⁴ , Hui Li^{1,3,5} , Kristopher G. Klein⁶ ,
Christopher J. Owen² , and Chi Wang^{1,3,5} 

¹ State Key Laboratory of Space Weather, National Space Science Center, Chinese Academy of Sciences, Beijing 100190, People's Republic of China; jiangwence@swl.ac.cn

² Mullard Space Science Laboratory, University College London, Dorking RH5 6NT, UK

³ Key Laboratory of Solar Activity and Space Weather, National Space Science Center, Chinese Academy of Sciences, Beijing 100190, People's Republic of China

⁴ Samsung Electronics Co. Ltd, Hwaseong, 18448, Republic of Korea

⁵ University of Chinese Academy of Sciences, Beijing, People's Republic of China

⁶ Department of Planetary Sciences, University of Arizona, Tucson, AZ, USA

Received 2023 October 8; revised 2023 October 23; accepted 2023 November 17; published 2023 December 20

Abstract

Wave–particle interactions play a crucial role in transferring energy between electromagnetic fields and charged particles in space and astrophysical plasmas. Despite the prevalence of different electromagnetic waves in space, there is still a lack of understanding of fundamental aspects of wave–particle interactions, particularly in terms of energy flow and velocity-space characteristics. In this study, we combine a novel quasilinear model with observations from the Magnetospheric Multiscale mission to reveal the signatures of resonant interactions between electrons and whistler waves in magnetic holes, which are coherent structures often found in the Earth's magnetosheath. We investigate the energy transfer rates and velocity-space characteristics associated with Landau and cyclotron resonances between electrons and slightly oblique propagating whistler waves. In the case of our observed magnetic hole, the loss of electron kinetic energy primarily contributes to the growth of whistler waves through the $n = -1$ cyclotron resonance, where n is the order of the resonance expansion in linear Vlasov–Maxwell theory. The excitation of whistler waves leads to a reduction of the temperature anisotropy and parallel heating of the electrons. Our study offers a new and self-consistent understanding of resonant energy transfer in turbulent plasmas.

Unified Astronomy Thesaurus concepts: [Solar wind \(1534\)](#); [Interplanetary turbulence \(830\)](#); [Space plasmas \(1544\)](#)

1. Introduction

Electromagnetic fluctuations in space and astrophysical plasmas expand across an extensive range of spatial and temporal scales (Tu & Marsch 1995; Alexandrova et al. 2013; Bruno & Carbone 2013; Verscharen et al. 2019b; Sahraoui et al. 2020). The interactions between charged particles and electromagnetic fluctuations play crucial roles for the energy conversion and dissipation in astrophysical plasma environments such as the solar wind, planetary magnetospheres, and the interstellar medium (Marsch 2006; Schekochihin et al. 2009). Resonant wave–particle interactions include Landau-resonant and cyclotron-resonant processes. They are efficient mechanisms to convert energy between electromagnetic fields and particles, causing particle acceleration/deceleration, the kinetic evolution of the particle velocity distribution function (VDF), and turbulence dissipation (Marsch et al. 1982; Gurnett & Reinleitner 1983; He et al. 2015; Xiao et al. 2015; Chen et al. 2019; Liu et al. 2022). Nonresonant wave–particle interactions include stochastic heating and magnetic reconnection in wave fields (Johnson & Cheng 2001; Voitenko & Goossens 2004; Chandran et al. 2010; Loureiro & Boldyrev 2017; Agudelo Rueda et al. 2021, 2022). To diagnose the signature of energy transfer in spacecraft observations, insightful techniques such as the field–particle correlation technique have been developed

and successfully implemented (Howes et al. 2017; Klein et al. 2017; Verniero et al. 2021; Montag et al. 2023). These methods reveal, for example, the dissipation of kinetic Alfvén waves through Landau damping in the Earth's magnetosheath (Chen et al. 2019; Verniero et al. 2021).

In the Earth's magnetosheath, enhanced electromagnetic fluctuations at kinetic scales such as whistler waves are sometimes localized near coherent structures like current sheets, magnetic islands, and magnetic holes (Zhang et al. 1998; Tsurutani et al. 2011; Karimabadi et al. 2014; Ahmadi et al. 2018; Breuillard et al. 2018; Behar et al. 2020; Kitamura et al. 2020; Li et al. 2021). These whistler waves are frequently observed as right-hand polarized electromagnetic waves with a small propagation angle with respect to the background magnetic field. Microinstabilities driven by unstable butterfly or beam-like VDFs are key candidates to explain the occurrence of these waves (Zhima et al. 2015; Ahmadi et al. 2018; Ren et al. 2019; Huang et al. 2020; Zhang et al. 2021). Although the direct observation of the energy transfer via cyclotron resonance is sometimes possible through data from the Magnetospheric Multiscale (MMS) mission (Kitamura et al. 2022), the understanding of the associated velocity-space signatures and the time-dependent properties of the resonant energy transfer between electrons and whistler waves is still lacking.

In this article, we focus on an interval previously studied by Jiang et al. (2022) and use a novel quasilinear model to numerically solve the quasilinear impact of wave–particle interactions on the temporal and energy evolution of the

plasma. We discuss the quantified signatures of energy transfer between whistler waves and electrons under the action of three different wave–particle resonance mechanisms. Finally, we provide suggestions for direct in situ observations of such resonant wave–particle interactions.

2. Quasilinear Evolution of the Distribution Function

Quasilinear theory describes the collective and slow (compared to the wave frequency) response of the VDF to fluctuating electromagnetic fields in resonant wave–particle interactions (Shapiro & Shevchenko 1962; Kennel & Engelmann 1966; Rowlands et al. 1966). In quasilinear theory, the time evolution of electron VDF via resonant interactions between electromagnetic fields and electrons (denoted by subscript e) follows a diffusion in velocity space:

$$\frac{\partial f_e}{\partial t} = \lim_{V \rightarrow \infty} \sum_{n=-\infty}^{\infty} \int \frac{\pi q_e^2}{V m_e^2} \hat{G}[k_{\parallel}] \times \left[\frac{v_{\perp}^2}{\|v_{\parallel}\|} \delta\left(k_{\parallel} - \frac{\omega_k - n\Omega_e}{v_{\parallel}}\right) \|\psi_e^n\|^2 \hat{G}[k_{\parallel}] f_e \right] d^3\mathbf{k}, \quad (1)$$

where f_e is the electron VDF,

$$\hat{G}[k_{\parallel}] = \left(1 - \frac{k_{\parallel} v_{\parallel}}{\omega_k}\right) \frac{1}{v_{\perp}} \frac{\partial}{\partial v_{\perp}} + \frac{k_{\parallel}}{\omega_k} \frac{\partial}{\partial v_{\parallel}}, \quad (2)$$

$$\psi_e^n = \frac{1}{\sqrt{2}} [E_k^R e^{i\phi} J_{n+1}(\rho_e) + E_k^L e^{-i\phi} J_{n-1}(\rho_e)] + \frac{v_{\parallel}}{v_{\perp}} E_k^z J_n(\rho_e), \quad (3)$$

q_e is the charge of an electron, m_e is the mass of an electron, k_{\parallel} is the wavevector component parallel to the background magnetic field \mathbf{B}_0 so that the full wavevector is decomposed as $\mathbf{k} = (k_{\perp} \cos \phi, k_{\perp} \sin \phi, k_{\parallel})$, v_{\perp} is the velocity component perpendicular to \mathbf{B}_0 , v_{\parallel} is the velocity component parallel to \mathbf{B}_0 , ω_k is the real part of the wave frequency, n is an integer ($n=0$ represents the Landau resonance and $n \neq 0$ represents cyclotron resonances), J_n is the Bessel function, $\rho_e = k_{\perp} v_{\perp} / \Omega_e$, $\Omega_e = q_e B_0 / (m_e c)$ is the electron cyclotron frequency, and c is the speed of light. In quasilinear theory, it is assumed that $|\gamma_k| \ll |\omega_k|$, where γ_k is the imaginary part of the wave frequency. We define the Fourier transformation of the electric field as $\mathbf{E}_k = (E_k^x, E_k^y, E_k^z)$ and its circular components as $E_k^R = (E_k^x - iE_k^y) / \sqrt{2}$ and $E_k^L = (E_k^x + iE_k^y) / \sqrt{2}$ (see also Verscharen et al. 2019a).

3. Method

3.1. Numerical Model for the Quasilinear Evolution

To investigate the time-dependent nature of quasilinear diffusion, we use a numerical model to solve the time evolution of electron VDFs according to Equation (1) (Jeong et al. 2020). Using a Crank–Nicolson scheme, the Jeong et al. (2020) model is a novel and generalized method to solve the time evolution of two-dimensional VDFs under the action of a dominant resonant wave–particle resonance.

In this model, we define approximate window functions to reflect the distribution of wave energy over k_{\parallel} (see

Jeong et al. 2020) as

$$W^n = \frac{1}{|v_{\parallel} - v_{g0}|} \exp \left[-\frac{k_{\parallel 0}^2}{\sigma_{\parallel 0}^2} \left(\frac{v_{\parallel} - v_{\parallel \text{res}}^n}{v_{\parallel} - v_{g0}} \right)^2 \right], \quad (4)$$

where

$$v_{\parallel \text{res}}^n = \frac{\omega_{k0} - n\Omega_e}{k_{\parallel 0}} \quad (5)$$

is the n th order resonance velocity, v_{g0} is the group velocity, $k_{\parallel 0}$ is the central parallel wavenumber, ω_{k0} is the central frequency, $\sigma_{\parallel 0}$ is the half-width of the window function, $v_{Ae} = B_0 / \sqrt{4\pi n_e m_e}$ is the electron Alfvén speed, and n_e is the electron number density. Equation (4) determines the region in v_{\parallel} space in which the quasilinear diffusion through the n th order resonance with unstable whistler waves is effective.

The width of the window function is determined by the unstable whistler-wave spectrum calculated with the Arbitrary Linear Plasma Solver (ALPS; Verscharen et al. 2018; Klein et al. 2023b). To determine the window functions, we implement a non-Maxwellian VDF model into ALPS to evaluate the stability of whistler waves. The VDF model is based on realistic electron VDF data from MMS1 on 2017 January 25 from 00:25:44.38 to 00:26:44.80 UT (more details see Jiang et al. 2022). Figure 1(b) shows isocontours of the initial electron VDF. ALPS predicts an unstable spectrum of whistler waves, i.e., $\gamma_k > 0$ in the range $0.5 < k_{\parallel} d_e < 0.8$, where d_e denotes the electron inertial length. Therefore, we set $\sigma_{\parallel 0} = 0.08 d_e$, $k_{\parallel 0} d_e = 0.64$, and $v_{g0} = 0.07 v_{Ae}$ in our numerical model. The unstable whistler waves have a propagation angle slightly oblique to the background magnetic field ($\sim 10^\circ$) and the real part of the frequency at maximum growth is $\omega_{k0} = 0.26 \Omega_e$, which is in agreement with the observed wave properties (Jiang et al. 2022). We determine the magnetic-field amplitude of whistler waves as 0.0018 nT from direct MMS observations (Torbert et al. 2016). In our model, the electron VDF is discretized into a 120×240 grid on the $(v_{\parallel}, v_{\perp})$ plane, where $-3v_{Ae} \leq v_{\parallel} \leq 3v_{Ae}$ and $0 \leq v_{\perp} \leq 3v_{Ae}$.

3.2. Trajectories of Quasilinear Diffusion

In Figure 1(a), we show the relevant W^n , which are defined to have their maximum at the resonance velocities according to Equation (5). We determine the directions of the diffusive flux of particles according to Equation (1) based on the local gradients of the velocity distribution function. The diffusive flux of particles in velocity space is locally tangent to concentric elliptical/hyperbolic curves around the point ($v_{\perp} = 0, v_{\parallel} = v_{g0}$) given by Jeong et al. (2020):

$$v_{\perp}^2 + \left[\frac{n\Omega_e}{n\Omega_e - \omega_{k0} + k_{\parallel 0} v_{g0}} \right] (v_{\parallel} - v_{g0})^2 = \text{const.} \quad (6)$$

Figure 1(b) shows the trajectories according to Equation (6) using colored curves with arrows for $n=0$ (blue), $n=1$ (green), and $n=-1$ (red). The arrows represent the directions of diffusive fluxes, which are always directed from larger values of f_e toward smaller values of f_e . Variations in the local gradients cause the direction of the diffusive flux for $n=0$ to change at different v_{\perp} as shown by the alternating blue arrows.

The direction of the diffusive flux at a specific point in velocity space is determined by the local gradient

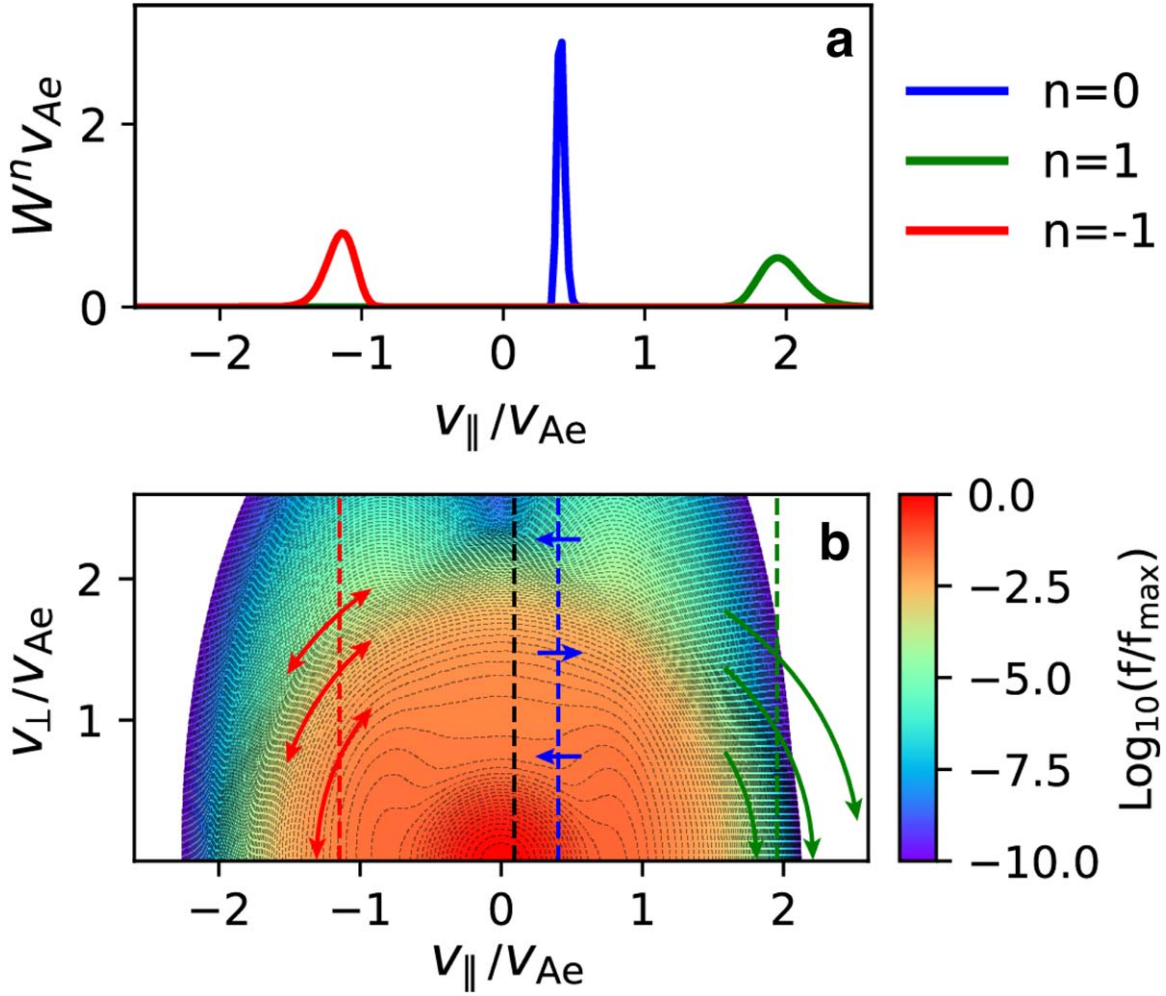


Figure 1. Quasilinear diffusion in velocity space and window functions for the unstable wave energy spectrum. (a) Window functions W^n as a function of $v_{||}$ for $n = 0$ (blue), $n = 1$ (green), and $n = -1$ (red) according to Equation (4). (b) Isocontours of our electron VDF fit in velocity space. The black (blue) vertical dashed line represents the group (phase) velocity of the whistler waves. The green and red vertical dashed lines represent $v_{||\text{res}}^{+1}$ and $v_{||\text{res}}^{-1}$. The colored arrows show the local direction of the flux of diffusing particles (blue: $n = 0$, green: $n = 1$, and red: $n = -1$) according to Equation (6) and the local gradient of the VDF.

$\hat{G}[k_{||}]f_e(v_{||}, v_{\perp})$ of the VDF. It determines whether the local quasilinear diffusion contributes to wave growth or to wave damping, and can significantly vary with v_{\perp} . If the particles lose kinetic energy during the diffusion, they contribute to the growth of the wave. If they gain energy, they contribute to its damping. Particles at different pitch angles and different energy can experience opposite effects given a specific fine structure of the VDF in velocity space. For example, around $v_{\perp} \approx 0.7v_{Ae}$ along the $n = 0$ resonance, f_e has a negative gradient in the $v_{||}$ direction, suggesting that the direction of the diffusive particle flux points into the negative $v_{||}$ direction. The corresponding electrons lose kinetic energy, which thus is transferred into the wave energy. However, electrons at $v_{\perp} \approx 1.5v_{Ae}$ diffuse in the opposite direction, thus absorbing wave energy. For $n = 1$, the diffusive particle flux is clockwise at $v_{||} \approx v_{||\text{res}}^{+1}$, leading to an increase in the kinetic energy of these electrons. This diffusion contributes to the damping of the whistler waves. For $n = -1$, the diffusive particle flux is counterclockwise at $v_{||} \approx v_{||\text{res}}^{-1}$, leading to a decrease in the kinetic energy of these electrons. This diffusion contributes to the growth of the whistler waves. Electrons at $v_{||} \gtrsim v_{||\text{res}}^{-1}$ diffuse toward larger kinetic energy and thus contribute to wave damping. The net gain or loss of energy

of all electrons defines whether the corresponding resonant mode undergoes growth or damping.

3.3. Resonant Energy Transfer in Velocity Space

Upon obtaining VDFs at different quasilinear evolution times, we evaluate the relative contributions of the three resonances to the energy conversion using the method presented by Howes et al. (2017). We first calculate the velocity-space energy density

$$w(v_{\perp}, v_{||}, t) = \frac{1}{2} m_e v^2 f_e(v_{\perp}, v_{||}, t) \quad (7)$$

and the two-dimensional energy transfer rate

$$C(v_{\perp}, v_{||}) = \frac{\partial w(v_{\perp}, v_{||}, t)}{\partial t}. \quad (8)$$

By performing partial integration, we obtain the one-dimensional energy transfer rates both in the parallel direction

$$C_{||}(v_{||}) = \int_0^{\infty} 2\pi v_{\perp} C(v_{\perp}, v_{||}) dv_{\perp} \quad (9)$$

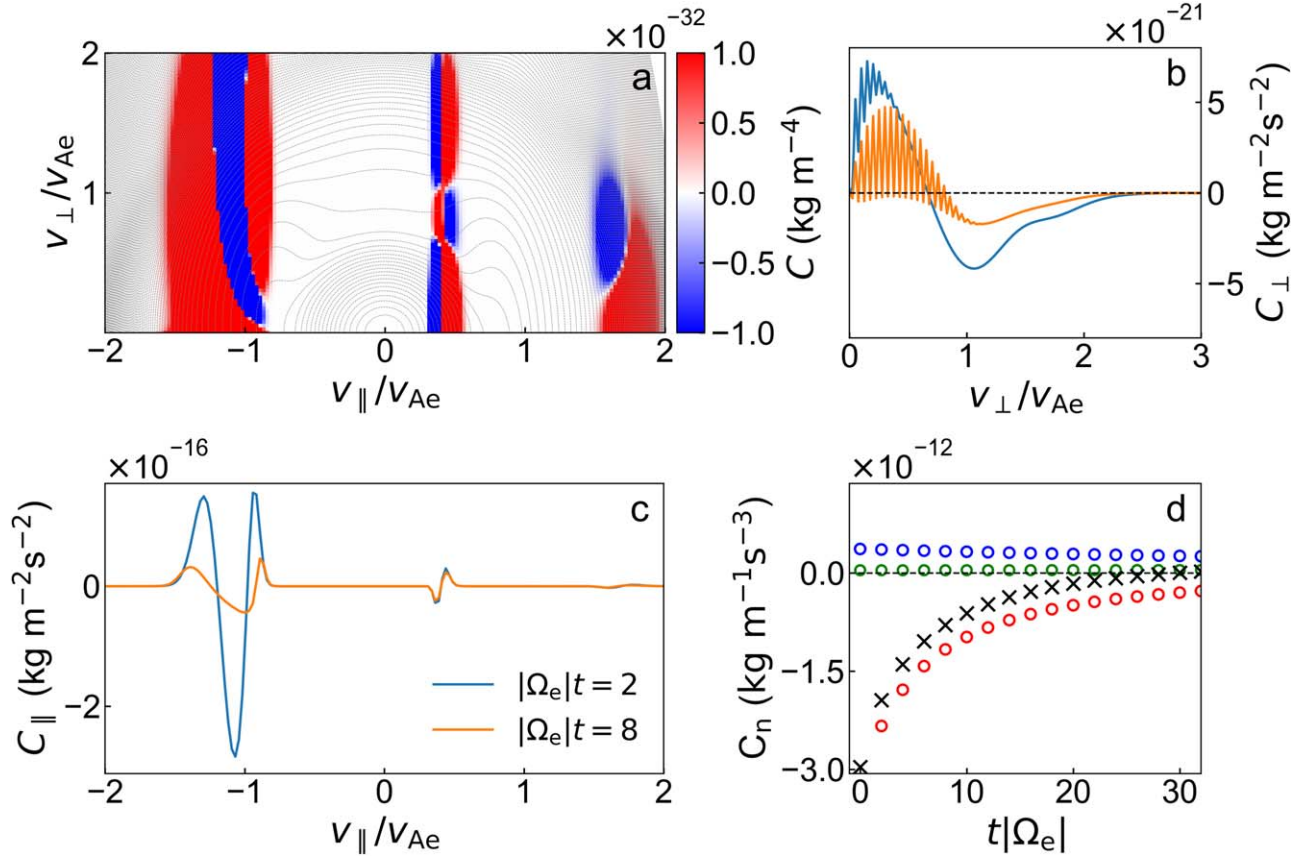


Figure 2. Energy transfer rates of resonant electron–whistler interactions predicted by our numerical model. (a) $C(v_{\perp}, v_{\parallel})$ at $t|\Omega_e| = 2$ as a function of v_{\parallel} and v_{\perp} . The background isocontours show the initial electron VDF. (b) $C_{\perp}(v_{\perp})$ as a function of v_{\perp} . (c) $C_{\parallel}(v_{\parallel})$ as a function of v_{\parallel} . (d) Time plots of the total energy transfer rate (black crosses) and the contributions from $n = -1$ (red circles), $n = 1$ (green circles), and $n = 0$ (blue circles). Blue curves in (b) and (c) represent the energy transfer rates at $t|\Omega_e| = 2$, and orange curves at $t|\Omega_e| = 8$.

and in the perpendicular direction

$$C_{\perp}(v_{\perp}) = \int_{-\infty}^{\infty} 2\pi v_{\perp} C(v_{\perp}, v_{\parallel}) dv_{\parallel}. \quad (10)$$

Moreover, we obtain the net energy transfer rate by a second integration over the remaining direction:

$$C_{\text{net}} = \int_{-\infty}^{\infty} C_{\parallel}(v_{\parallel}) dv_{\parallel} = \int_0^{\infty} C_{\perp}(v_{\perp}) dv_{\perp}. \quad (11)$$

To compare contributions from different resonances, we define the energy transfer rates for different orders n as

$$C_n = \int_{v_{\parallel, \text{res}}^-}^{v_{\parallel, \text{res}}^+} C_{\parallel}(v_{\parallel}) dv_{\parallel}, \quad (12)$$

where w_n is the half-width of the effective v_{\parallel} range for the resonant interaction of n th order.

4. Result

4.1. Velocity-space Signature of Energy Transfer

Figure 2(a) shows $C(v_{\perp}, v_{\parallel})$ in the $(v_{\perp}, v_{\parallel})$ -plane. The isocontours represent the initial VDF, while the color represents the magnitude of $C(v_{\perp}, v_{\parallel})$ at time $t|\Omega_e| = 2$. We show $C_{\perp}(v_{\perp})$ in Figure 2(b) and $C_{\parallel}(v_{\parallel})$ in Figure 2(c). Different colored lines in panels (b) and (c) of Figure 2 represent the transfer rates at $t|\Omega_e| = 2$ (blue) and $t|\Omega_e| = 8$ (orange). Figure 2(d) shows C_{net} , C_0 , C_{-1} , and C_{+1} as functions of time.

Both one-dimensional energy conversion rates show a strong dependence on v_{\parallel} and v_{\perp} . According to Figure 2(a), $C(v_{\perp}, v_{\parallel})$ shows an alternating pattern in velocity space. For $n = 0$, $C(v_{\perp}, v_{\parallel})$ shows the expected bipolar double-band signature along the v_{\parallel} direction, which when integrated contributes to the damping of the whistler waves. However, this bipolar signature reverses at $v_{\perp} \approx v_{Ae}$ due to reversed velocity gradients of the electron VDFs along v_{\parallel} (see also Figure 2(c)). The reversed bipolar part of $C(v_{\perp}, v_{\parallel})$ contributes to the growth of the whistler waves. As shown by the blue circles in Figure 2(d), the $n = 0$ resonance overall makes a damping contribution to the whistler-wave evolution. For $n = 1$, $C(v_{\perp}, v_{\parallel})$ shows a velocity-space pattern consistent with the diffusive paths shown in Figure 1(b). At $v_{\parallel} \approx v_{\parallel, \text{res}}^{+1}$, the diffusive flux is directed toward larger v^2 , suggesting an increase in kinetic energy of the resonant electrons. While $|C_{+1}| \ll |C_0|$, the $n = 1$ resonance also contributes to the damping of the whistler instability.

The $n = -1$ resonance produces a triple-band signature in $C(v_{\perp}, v_{\parallel})$. This signature indicates that the electrons with $v_{\parallel} \approx v_{\parallel, \text{res}}^{-1}$ diffuse along both possible directions shown in Figures 1(b) and 2(a). Inspecting $C_{\parallel}(v_{\parallel})$ in Figure 2(c) suggests that the electrons with $v_{\parallel} \approx v_{\parallel, \text{res}}^{-1}$ overall lose kinetic energy, contributing to the growth of whistler waves. The loss of kinetic energy through the $n = -1$ resonance is greater than the combined gain of kinetic energy through the $n = 0$ and $n = 1$ resonances. According to Figure 2(d), the contribution of the $n = -1$ resonance is the dominant source for the growth of whistler instability.

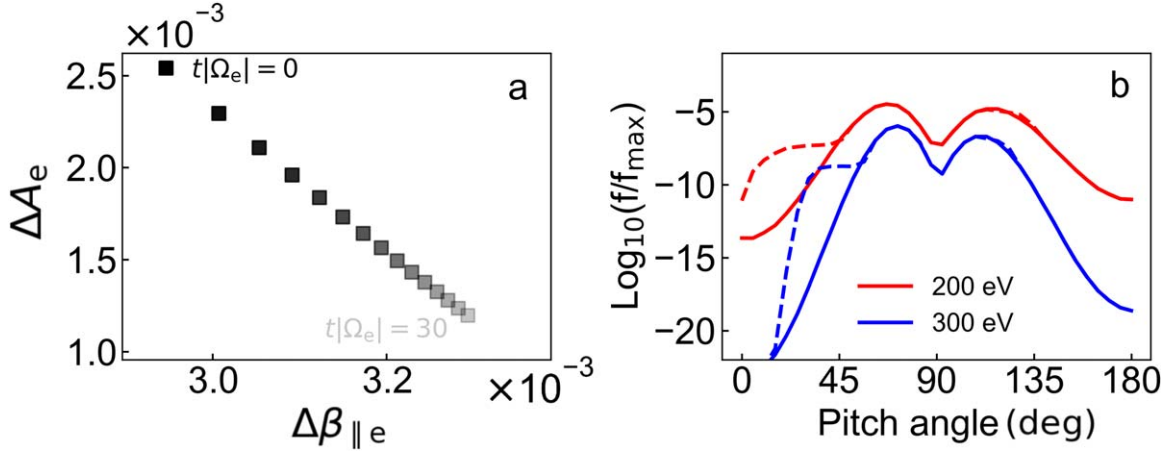


Figure 3. Joint time evolution of ΔA_e and $\Delta \beta_{||e}$. (a) Evolution of ΔA_e and $\Delta \beta_{||e}$ at different times. (b) Pitch-angle distributions for 200 eV (red) and 300 eV (blue) electrons. Solid and dotted curves represent distributions at $t|\Omega_e| = 0$ and $t|\Omega_e| = 30$.

4.2. Quasilinear Saturation and Stabilization

During the time evolution according to Equation (1), the magnitudes of $C_{\perp}(v_{\perp})$ and $C_{||}(v_{||})$ decrease. This result suggests that the diffusion caused by whistler waves slows down, which is a result of the decrease in the local velocity gradients of the VDFs. This secular effect is the quasilinear saturation mechanism of the whistler-wave instability under consideration. By integrating over all velocities, we obtain the net energy transfer rates at $t|\Omega_e| = 2$ as $C_{-1} \approx -1.87 \times 10^{-12} \text{ kg m}^{-1} \text{ s}^{-3}$, $C_0 \approx 1.65 \times 10^{-13} \text{ kg m}^{-1} \text{ s}^{-3}$, and $C_{+1} \approx 2.45 \times 10^{-14} \text{ kg m}^{-1} \text{ s}^{-3}$. We obtain a net energy transfer rate of $C_{\text{net}} \approx 1.68 \times 10^{-12} \text{ kg m}^{-1} \text{ s}^{-3}$. As shown in Figure 2(d), the net energy transfer rates gradually decrease with time, indicating quasilinear saturation of the system. Therefore, we conclude that the $n = -1$ cyclotron resonance drives the growth of the whistler waves, while the $n = 0$ Landau resonance and the $n = 1$ cyclotron resonance lower their growth rate.

Figure 3(a) presents the time evolution of ΔA_e and $\Delta \beta_{||e}$, which are the differences between A_e and $\beta_{||e}$ and their initial values. $A_e = T_{\perp e}/T_{||e}$ and $\beta_{||e}$ are calculated as the moments of the VDFs in our quasilinear model. From $t|\Omega_e| = 0$ to $t|\Omega_e| = 30$, A_e decreases and $\beta_{||e}$ increases as a result of the action of the discussed resonant wave–particle interactions. The parametric variation of A_e and $\beta_{||e}$ gradually decreases as the overall velocity gradients in the resonance regions decrease. The increase in $\beta_{||e}$ with time is directly related to the increase in $T_{||e}$, which is the result of the quasilinear diffusion in velocity space. The velocity-space morphology of the electron beam configuration at energies between 200 and 300 eV is noticeably weakened and evolves toward a more isotropic distribution (see Figure 3(b)). The major contribution to the energy transfer is from regions with high phase-space densities. While the contribution of the $n = 1$ resonance to the total energy transfer is small, its role in reshaping the distribution in regions of velocity space with small phase-space densities is still important.

4.3. Virtual Observations of Velocity-space Signatures

To guide future in situ observations of similar signatures, we interpolate our result from Figure 2(a) onto energy-angle grids with a logarithmic energy table of a virtual spacecraft. As an example, we demonstrate our results for two sets of energy-angle resolutions ($\Delta\theta = 11.25^\circ$, $\Delta E/E = 13\%$; and $\Delta\theta = 4^\circ$,

$\Delta E/E = 14\%$), which are shown in Figure 4. For the virtual instrument, we define the pitch angle as θ and the energy as E . We assume that the background magnetic-field direction is aligned with the axis when best pitch-angle resolution is achieved. The chosen energy-angle resolutions are selected according to typical values for the electrostatic analyzer onboard Solar Orbiter Electron Analyzer System (Figure 4(a)) (Owen et al. 2020) and MMS Fast Plasma Investigation (Figure 4(b); Pollock et al. 2016).

As $\Delta E/E$ and $\Delta\theta$ decrease, the signatures of the three resonances in velocity space become more pronounced and thus easier to identify. With decreasing pitch-angle resolution, the morphological features of the two-dimensional energy transfer rate become increasingly difficult to distinguish. Nevertheless, the range of wave–particle resonances are variable depending on the wave parameters.

5. Discussion and Conclusions

Based on our MMS observations of the electron VDF in a magnetic hole, we combine linear Vlasov–Maxwell theory and a quasilinear numerical model to investigate the properties of wave–particle interactions between electrons and whistler waves. Our method reveals the velocity-space signatures of energy transfer in these resonant interactions. We quantify the relative contributions of different resonances ($n = 0$, $n = -1$, and $n = 1$) to the energy transfer rate in velocity space. The energy conversion rate for the $n = -1$ cyclotron resonance is the dominant contribution to the whistler-wave instability, followed by the damping contributions from the $n = 0$ Landau resonance and the $n = +1$ cyclotron resonance. The net energy transfer from the three resonances is $C_{\text{net}} \approx 1.30 \times 10^{-12} \text{ kg m}^{-1} \text{ s}^{-3}$. The net energy transfer from electron kinetic energy to whistler-wave energy leads to the growth of the observed electron–whistler wave instability. Furthermore, our results reveal significant dependencies of quasilinear diffusion on the local velocity-space structures of the VDFs, which gives rise to complicated patterns of energy transfer in velocity space.

Our results present complex velocity-space signatures of resonant energy transfer between unstable whistler waves and electrons. We interpolate these signatures into finite phase-space bins similar to the operating principle of recent spacecraft instrumentation such as those onboard MMS (Pollock et al. 2016) and Solar Orbiter (Owen et al. 2020). The angular and

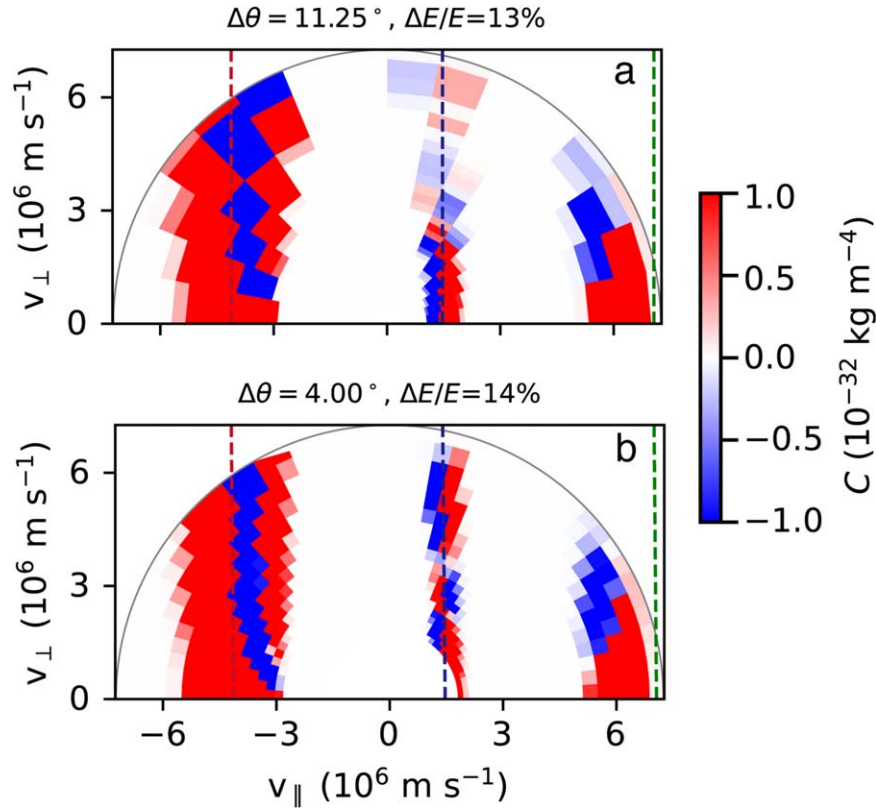


Figure 4. Velocity-space signatures of energy transfer rates interpolated for different pitch-angle resolutions and energy resolutions of a particle instrument on a virtual spacecraft. We interpolate $C(v_{\parallel}, v_{\perp})$ onto energy-angle grids with a resolution of (a) $\Delta\theta = 11.25^{\circ}$, $\Delta E/E = 13\%$, and (b) $\Delta\theta = 4^{\circ}$, $\Delta E/E = 14\%$. The blue, red, and green dashed lines represent $v_{\parallel, \text{res}}^0$, $v_{\parallel, \text{res}}^{-1}$, and $v_{\parallel, \text{res}}^{+1}$, respectively.

energy resolution of the two instruments is sufficient for direct measurement of resonant energy transfer in velocity space. However, a significant undersampling issue would affect the measurement if the timescale of resonant diffusion is much smaller than the time resolution of the instrument (Verniero et al. 2021; Horvath et al. 2022; Wilson et al. 2022). We also acknowledge that the used angle/energy resolutions in Section 4.3 are simplified to some extent. The resolution of pitch angles depends on the orientation of the magnetic-field direction with respect to the the instrument frame due to the conversion of instrument-frame angles (azimuth/elevation) into pitch angles. In the case of MMS, for example, the pitch-angle resolution varies between 4° and 11.25° depending on the orientation of the magnetic field. The direct measurement of fast diffusion created by high-frequency whistler waves is still a major challenge that can potentially benefit from novel instrument concepts that focus on electron-scale wave-particle interactions. Our method, applied to high-resolution particle data from present and future missions such as Solar Orbiter, MMS, and HelioSwarm (Klein et al. 2023a), is a helpful tool to investigate wave-particle interactions and their impact on VDFs both for electrons and ions.

Acknowledgments

The Arbitrary Linear Plasma Solver (ALPS) code is publicly available at <https://github.com/danielver02/ALPS>, and the ALPS documentation can be found at <http://alps.space>. The ALPS project received support from UCLs Advanced Research Computing Centre through the Open Source Software Sustainability Funding scheme. This research was supported by the

International Space Science Institute (ISSI) in Bern, through ISSI International Team project No. 563 (Ion Kinetic Instabilities in the Solar Wind in Light of Parker Solar Probe and Solar Orbiter Observations) led by L. Ofman and L. Jian. This work is supported by NNSFC grants (42022032, 42374198, 41874203, 42188101), project of Civil Aerospace “13th Five Year Plan” Preliminary Research in Space Science (D020301). D.V. is supported by the STFC Ernest Rutherford Fellowship ST/P003826/1 and STFC Consolidated grants ST/S000240/1 and ST/W001004/1. H.L. is supported by the International Partnership Program of CAS (grant No. 183311KYSB20200017) and in part by the Specialized Research Fund for State Key Laboratories of China. K.G.K. is supported by grant DE-SC0020132 and NASA ECIP 80NSSC19K0912.

ORCID iDs

Wence Jiang <https://orcid.org/0000-0001-7431-5759>
 Daniel Verscharen <https://orcid.org/0000-0002-0497-1096>
 Seong-Yeop Jeong <https://orcid.org/0000-0001-8529-3217>
 Hui Li <https://orcid.org/0000-0002-4839-4614>
 Kristopher G. Klein <https://orcid.org/0000-0001-6038-1923>
 Christopher J. Owen <https://orcid.org/0000-0002-5982-4667>
 Chi Wang <https://orcid.org/0000-0001-6991-9398>

References

Agudelo Rueda, J. A., Verscharen, D., Wicks, R. T., et al. 2021, *JPIPh*, **87**, 905870228
 Agudelo Rueda, J. A., Verscharen, D., Wicks, R. T., et al. 2022, *ApJ*, **938**, 4

- Ahmadi, N., Wilder, F. D., Ergun, R. E., et al. 2018, *JGRA*, **123**, 6383
- Alexandrova, O., Chen, C. H. K., Sorriso-Valvo, L., Horbury, T. S., & Bale, S. D. 2013, *SSRv*, **178**, 101
- Behar, E., Sahraoui, F., & Berčić, L. 2020, *JGRA*, **125**, e28040
- Breuillard, H., Le Contel, O., Chust, T., et al. 2018, *JGRA*, **123**, 93
- Bruno, R., & Carbone, V. 2013, *LRSP*, **10**, 2
- Chandran, B. D. G., Li, B., Rogers, B. N., Quataert, E., & Germaschewski, K. 2010, *ApJ*, **720**, 503
- Chen, C. H. K., Klein, K. G., & Howes, G. G. 2019, *NatCo*, **10**, 740
- Gurnett, D. A., & Reinleitner, L. A. 1983, *GeoRL*, **10**, 603
- He, J., Tu, C., Marsch, E., et al. 2015, *ApJL*, **813**, L30
- Horvath, S. A., Howes, G. G., & McCubbin, A. J. 2022, *PhPI*, **29**, 062901
- Howes, G. G., Klein, K. G., & Li, T. C. 2017, *JPIPh*, **83**, 705830102
- Huang, S. Y., Xu, S. B., He, L. H., et al. 2020, *GeoRL*, **47**, e87515
- Jeong, S.-Y., Verscharen, D., Wicks, R. T., & Fazakerley, A. N. 2020, *ApJ*, **902**, 128
- Jiang, W., Verscharen, D., Li, H., Wang, C., & Klein, K. G. 2022, *ApJ*, **935**, 169
- Johnson, J. R., & Cheng, C. Z. 2001, *GeoRL*, **28**, 4421
- Karimabadi, H., Roytershteyn, V., Vu, H. X., et al. 2014, *PhPI*, **21**, 062308
- Kennel, C. F., & Engelmann, F. 1966, *PhFl*, **9**, 2377
- Kitamura, N., Amano, T., Omura, Y., et al. 2022, *NatCo*, **13**, 6259
- Kitamura, N., Omura, Y., Nakamura, S., et al. 2020, *JGRA*, **125**, e27488
- Klein, K. G., Howes, G. G., & TenBarge, J. M. 2017, *JPIPh*, **83**, 535830401
- Klein, K. G., Spence, H., Alexandrova, O., et al. 2023a, *SSRv*, **219**, 74
- Klein, K. G., Verscharen, D., Koskela, T., & Stansby, D. 2023b, The Arbitrary Linear Plasma Solver, v1.0.1, Zenodo, doi:10.5281/zenodo.8075682
- Li, J.-H., Zhou, X.-Z., Zong, Q.-G., et al. 2021, *GeoRL*, **48**, e91613
- Liu, Z.-Y., Zong, Q.-G., Rankin, R., et al. 2022, *NatCo*, **13**, 5593
- Loureiro, N. F., & Boldyrev, S. 2017, *ApJ*, **850**, 182
- Marsch, E. 2006, *LRSP*, **3**, 1
- Marsch, E., Mühlhäuser, K.-H., Schwenn, R., et al. 1982, *JGR*, **87**, 52
- Montag, P., Howes, G., McGinnis, D., et al. 2023, arXiv:2306.09061
- Owen, C. J., Bruno, R., Livi, S., et al. 2020, *A&A*, **642**, A16
- Pollock, C., Moore, T., Jacques, A., et al. 2016, *SSRv*, **199**, 331
- Ren, Y., Dai, L., Li, W., et al. 2019, *GeoRL*, **46**, 5045
- Rowlands, J., Shapiro, V. D., & Shevchenko, V. I. 1966, *JETP*, **23**, 651
- Sahraoui, F., Hadid, L., & Huang, S. 2020, *RvMPP*, **4**, 4
- Schekochihin, A. A., Cowley, S. C., Dorland, W., et al. 2009, *ApJS*, **182**, 310
- Shapiro, V., & Shevchenko, V. 1962, *ZhETF*, **42**
- Torbert, R. B., Russell, C. T., Magnes, W., et al. 2016, *SSRv*, **199**, 105
- Tsurutani, B. T., Lakhina, G. S., Verkhoglyadova, O. P., et al. 2011, *JGRA*, **116**, A02103
- Tu, C. Y., & Marsch, E. 1995, *SSRv*, **73**, 1
- Verniero, J. L., Howes, G. G., Stewart, D. E., & Klein, K. G. 2021, *JGRA*, **126**, e28361
- Verscharen, D., Chandran, B. D. G., Jeong, S.-Y., et al. 2019, *ApJ*, **886**, 136
- Verscharen, D., Klein, K. G., Chandran, B. D. G., et al. 2018, *JPIPh*, **84**, 905840403
- Verscharen, D., Klein, K. G., & Maruca, B. A. 2019b, *LRSP*, **16**, 5
- Voitenko, Y., & Goossens, M. 2004, *ApJL*, **605**, L149
- Wilson, L. B., Goodrich, K. A., Turner, D. L., et al. 2022, *FrASS*, **9**, 1063841
- Xiao, F., Yang, C., Su, Z., et al. 2015, *NatCo*, **6**, 8590
- Zhang, H., Zhong, Z., Tang, R., et al. 2021, *GeoRL*, **48**, e96056
- Zhang, Y., Matsumoto, H., & Kojima, H. 1998, *JGR*, **103**, 4615
- Zhima, Z., Cao, J., Fu, H., et al. 2015, *JGRA*, **120**, 2469